Cellular mechanisms of spatial navigation in the medial entorhinal cortex

Christoph Schmidt-Hieber[1,2] & Michael Häusser[1,2]

Neurons in the medial entorhinal cortex exhibit a grid-like spatial pattern of spike rates that has been proposed to represent a neural code for path integration. To understand how grid cell firing arises from the combination of intrinsic conductances and synaptic input in medial entorhinal stellate cells, we performed patch-clamp recordings in mice navigating in a virtual-reality environment. We found that the membrane potential signature of stellate cells during firing field crossings consisted of a slow depolarization driving spike output. This was best predicted by network models in which neurons receive sustained depolarizing synaptic input during a field crossing, such as continuous attractor network models of grid cell firing. Another key feature of the data, phase precession of intracellular theta oscillations and spiking with respect to extracellular theta oscillations, was best captured by an oscillatory interference model. Thus, these findings provide crucial new information for a quantitative understanding of the cellular basis of spatial navigation in the entorhinal cortex.

The majority of principal cells in layer II of the medial entorhinal cortex (MEC) have multiple firing fields that form a hexagonal grid spanning the environment of a navigating animal[1–3]. As an animal approaches the center of a firing field, spikes not only increase in frequency, but also occur at successively earlier phases of the local field potential theta[4,5]. This combined rate and phase precession code has captured the attention of both theorists and experimentalists, as it may represent a neural mechanism for path integration[1,6,7].

Several models have been proposed to explain how grid cell firing emerges from cellular and network properties. In one class of models, grid cell firing is the result of temporal interference between several membrane potential oscillations whose frequencies are differentially modulated in the theta frequency range (5–12 Hz) by animal speed and running direction[8–10]. The underlying velocity-controlled oscillators (VCOs) could originate from either intrinsic conductances or external inputs to a grid cell[8]. In either case, these oscillatory interference models predict that spikes are produced when the VCOs are in phase with each other during a firing field crossing. Another class of grid cell firing models is based on a continuous attractor network (CAN) of neurons. Recurrent synaptic connectivity with a center-surround synaptic weight profile can lead to the formation of periodic activity bumps in a neural sheet. Grid cell firing emerges when the neural activity in this sheet is coupled to an additional layer of velocity-sensitive neurons, leading to sustained net excitation in a grid cell during a firing field crossing[6,7,11,12].

Although these models make contrasting predictions about how single neurons convert synaptic inputs into grid cell firing, we currently lack direct recordings of membrane potential from MEC neurons in navigating animals, which would allow us to constrain and discriminate between the different models. Thus, we performed whole-cell patch-clamp recordings from MEC neurons in mice navigating on a spherical treadmill surrounded by a virtual-reality environment. We found that the spiking mechanism during firing field crossings in stellate cells is best explained by a network model that produces sustained depolarizations, whereas the phase code is captured by an oscillatory interference model of grid cell firing.

RESULTS

Whole-cell recordings from MEC neurons in navigating mice

To obtain whole-cell patch-clamp recordings from MEC neurons in navigating mice, we developed a virtual-reality setup that allowed head-restrained mice to navigate on a spherical treadmill[13,14] (**Fig. 1a–c** and **Supplementary Video 1**). The virtual-reality scene was projected onto a spherical dome screen that covered nearly the entire field of view of the mouse. The complete projection apparatus was located underneath the mouse. When mice navigated on a rectangular track in this virtual reality environment, extracellular unit recordings from layer II of MEC exhibited multi-peaked firing fields (**Supplementary Fig. 1**). Firing occurred reproducibly during multiple runs in different directions across the firing field, consistent with spatial modulation of neuronal activity[3,15].

We then performed intracellular whole-cell recordings from stellate cells, pyramidal cells and fast-spiking neurons in MEC (**Fig. 1d–h** and **Supplementary Figs. 2–4**). We focused our attention primarily on stellate cells in layer II of MEC, where most pure grid cells are found[2]. Stellate cells were identified according to their electrophysiological signature[16,17] ($n = 26$) and, in some cases, their identity was confirmed by the characteristic morphology of biocytin-filled cells (**Fig. 1d,e** and **Supplementary Fig. 2**). Spontaneous firing rates in resting mice were low (0.3 ± 0.1 Hz, $n = 16$ stellate cells), and five stellate cells (31%) did not fire spontaneously at all (**Fig. 1f–h**).

[1]Wolfson Institute for Biomedical Research, University College London, London, UK. [2]Department of Neuroscience, Physiology and Pharmacology, University College London, London, UK. Correspondence should be addressed to C.S.-H. (c.schmidt-hieber@ucl.ac.uk) or M.H. (m.hausser@ucl.ac.uk).
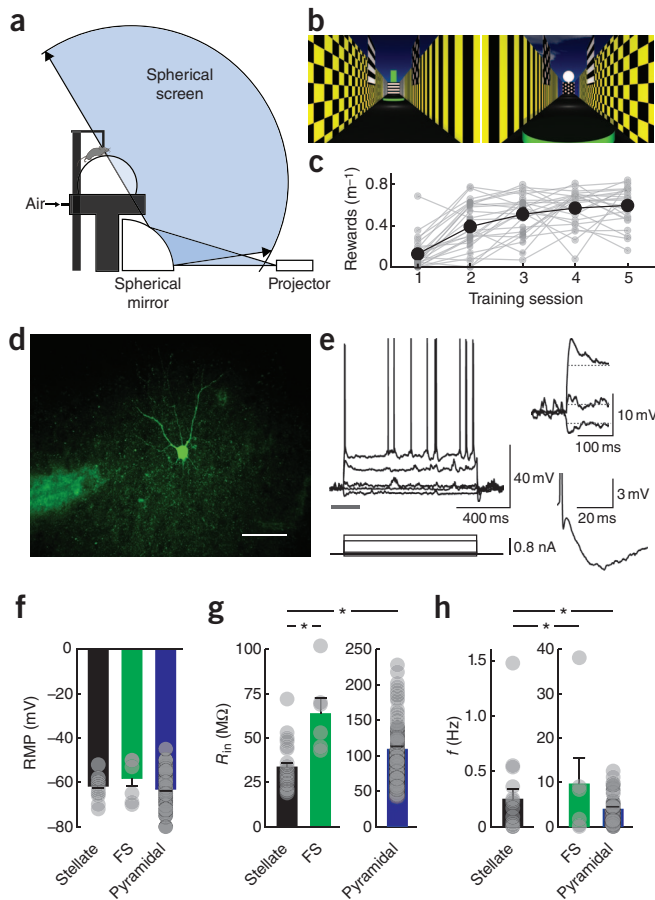
Figure 1 Patch-clamp recordings from MEC neurons in navigating mice. (**a**) Schematic of the virtual reality setup. (**b**) Two views in the virtual reality environment along the long axis of the track. (**c**) Improvement in performance during successive training sessions, assessed by number of equidistantly spaced rewards collected per meter on the virtual reality track. Gray circles represent individual mice and black circles represent the average. (**d**) Fluorescence image of a biocytin-filled stellate cell in layer II of dorsal MEC. Scale bar represents 50 μm. (**e**) Sub- and suprathreshold responses to injected current pulses in a stellate cell. The insets show positive and negative membrane potential sag (top; dashed lines indicate steady-state voltage) and an action potential (bottom) at higher magnification. (**f**–**h**) Bar graphs summarizing resting membrane potential (RMP; -62 ± 1 mV, mean $\pm$ s.e.m., ($n = 26$) versus -58 ± 4 mV ($n = 7$, $P = 0.38$) versus -63 ± 1 mV ($n = 111$, $P = 0.22$), **f**), input resistance (R_{in}; 34 ± 3 MΩ ($n = 26$) versus 64 ± 9 MΩ ($n = 6$, $P < 0.005$) versus 109 ± 4 MΩ ($n = 110$, $P < 10^{-4}$), **g**) and spontaneous firing frequency (f; 0.3 ± 0.1 Hz ($n = 16$) versus 9.6 ± 5.9 Hz ($n = 6$, $P < 0.05$) versus 3.8 ± 0.6 Hz ($n = 38$, $P < 10^{-4}$), **h**) in stellate, fast-spiking (FS) and putative pyramidal neurons of MEC. *$P < 0.05$ for comparisons with stellate cells. Error bars denote s.e.m.

Stellate cells exhibit theta oscillations during running

Stellate cells have been shown to exhibit pronounced spontaneous membrane potential oscillations (MPO$_\theta$) in the theta frequency range (5–12 Hz) in vitro[16,18], and these oscillations have been incorporated into some oscillatory interference models[18]. However, in awake resting mice, we did not observe any distinct theta periodicity at resting membrane potential or when depolarizing stellate cells close to spike threshold ($n = 15$; **Fig. 2** and **Supplementary Fig. 5a–c**), which is consistent with the idea that strong synaptic input in vivo may dampen such intrinsic oscillations[19]. Accordingly, input resistance in vivo was lower than previously reported for stellate cells in adult mice in vitro (34 versus 44 M Ω; ref. 20).

We next recorded stellate cell membrane potential while mice were navigating in the virtual reality environment to assess spatial modulation of membrane potential dynamics and firing. Stellate cells exhibit strong theta periodicity of membrane potential during local field potential (LFP) theta periods in vivo in anesthetized rats[21]. Similarly, in contrast to when mice were resting, we observed pronounced theta periodicity of membrane potential when mice were running (**Fig. 3a–d**), and a distinct theta peak appeared in the power spectrum that was substantially less pronounced in putative pyramidal neurons of the MEC (**Fig. 3e,f** and **Supplementary Fig. 5d–g**). Theta membrane potential oscillations preceded the onset of running, in some cases by more than one second (**Fig. 3a,b** and **Supplementary Fig. 2h**).

Sustained depolarizations drive stellate cell firing

During single runs along the track, stellate cells showed multi-peaked, periodic increases of firing rates (**Fig. 4a–d**), similar to grid cell firing in extracellular recordings from rats running on a linear track[15]
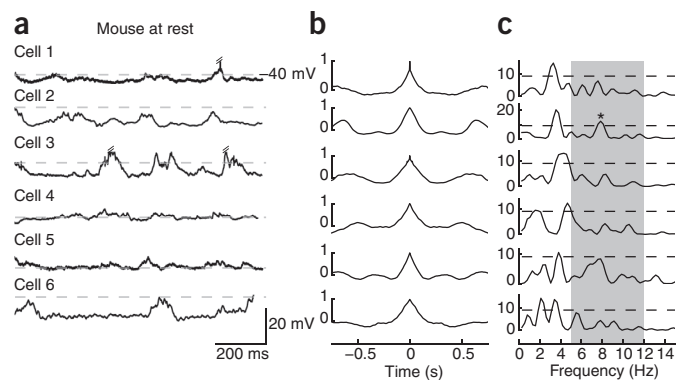
(mean field spacing = 58 ± 16 cm, mean field diameter = 20 ± 2 cm, mean peak firing rate = 10 ± 2 Hz, $n = 14$ fields in 6 stellate cells). Both spikes and MPO$_\theta$ showed a similar amount of phase precession with reference to simultaneously recorded LFP theta (phase precession slope for spikes: $-137°$ per field, $r = -0.14$, $P < 0.05$; for MPOs: $-147°$ per field, $r = -0.13$, $P < 0.05$). Consistently, spikes were in phase with MPO$_\theta$ during field crossings (phase precession slope = $4°$ per field, $r = 0.01$, $P = 0.78$, $n = 12$ fields from 5 stellate cells; **Fig. 4e** and **Supplementary Fig. 6**). Firing rate increases during field crossings were driven by slow membrane potential depolarizations that were sustained throughout the firing field and had an amplitude of 5.0 ± 1.0 mV ($n = 14$ fields in 6 stellate cells; **Figs. 4–6** and **Supplementary Figs. 7** and **8**). The amplitude of these sustained depolarizations depended on the initial membrane potential when entering a firing field: as the initial membrane potential was more depolarized, the amplitude of the depolarizations decreased (**Supplementary Fig. 8j**), suggesting that the distance from firing threshold in each cell can explain the range of values that we observed (0.3–12 mV; **Fig. 6b**). The amplitude of MPO$_\theta$ increased by only 2.0 ± 0.2 mV in the center of a firing field (**Figs. 4f** and **6b**, and **Supplementary Figs. 7** and **8**), suggesting that depolarization-driven firing could not be explained by

Figure 2 Stellate cell membrane potential shows no prominent theta periodicity in resting mice. (**a**) Representative membrane potential traces from six stellate cells recorded in awake, resting mice. Cells were depolarized close to spike threshold by sustained current injections. (**b**) Autocorrelograms corresponding to the traces shown in **a**. (**c**) Lomb spectra corresponding to membrane potential traces in **a**. Dashed lines indicate a significance value of 0.01. Asterisk indicates significant peaks ($P < 0.01$) in the theta frequency band (gray shaded area)[36].
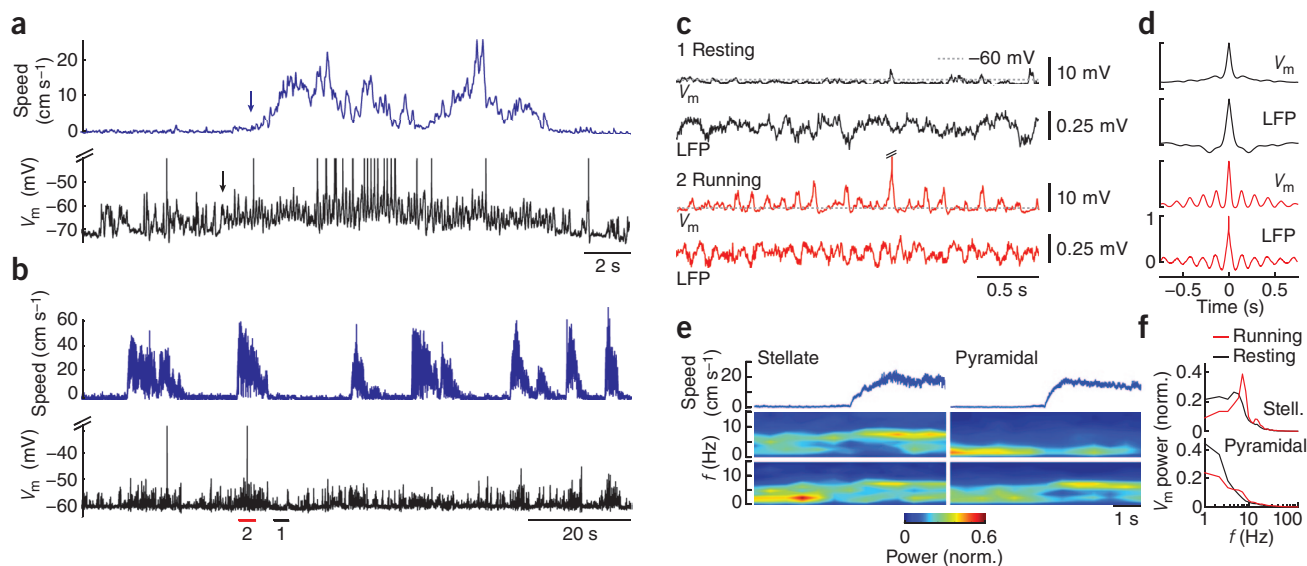
Figure 3 Stellate cells exhibit theta membrane potential oscillations during running. (**a**) Mouse speed (blue) and membrane potential of a stellate cell (black) during a running period. Note that onset of oscillatory activity (black arrow) precedes onset of running (blue arrow). (**b**) Mouse speed (blue) and membrane potential of another stellate cell (black) during navigation in the virtual reality environment. (**c**) Membrane potential of a stellate cell and simultaneously recorded LFP when the mouse is resting (black) and during running (red). The traces were taken from the recording shown in **b**, as indicated by horizontal bars at the bottom of **b**. (**d**) Autocorrelograms of membrane potential and LFP during the resting (black) and running (red) periods shown in **c**. (**e**) Spectrograms of membrane potential (middle) and LFP (bottom) were normalized and aligned to the onset of movement (top) before computing the average for stellate cells (left, $n = 9$) and putative pyramidal cells (right, $n = 24$). (**f**) Average power spectra for stellate cells (top) and putative pyramidal cells (bottom) at rest (black) and while running (red).

changes in MPO_θ alone. Indeed, we found that action potential firing rates strongly depended on slow changes in membrane potential below the theta frequency range, whereas changes in MPO_θ amplitudes were only weakly correlated with firing rates (**Fig. 6a**).

CAN models reproduce the firing mechanism

To assess how our experimental data compare to predictions of existing grid cell models, we first implemented a standard oscillatory interference model[8] using a detailed compartmental model of a stellate cell (**Fig. 5**).
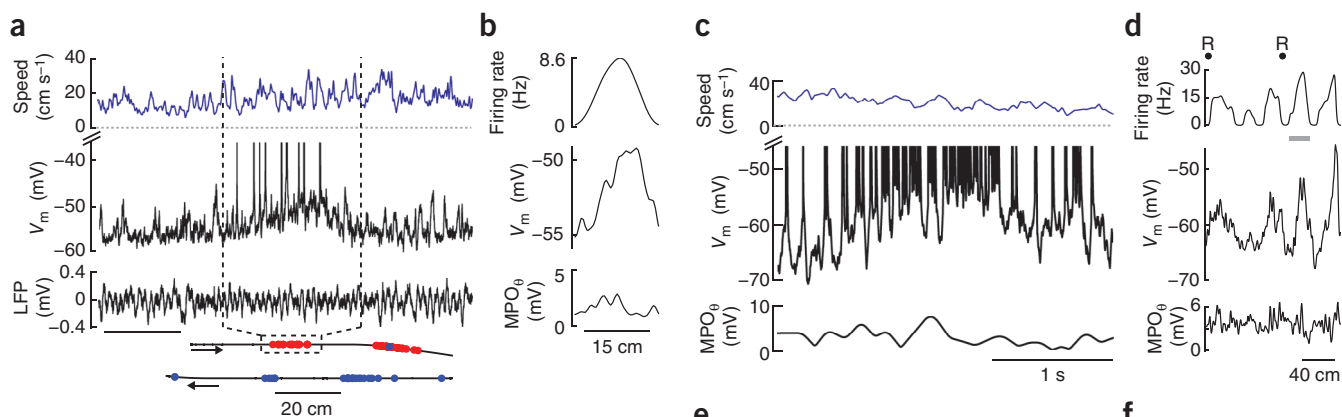

Figure 4 Sustained depolarizations drive stellate cell firing. (**a**) Mouse speed (top), membrane potential of a stellate cell (middle) and LFP (bottom) during a firing field crossing. The corresponding trajectory of the mouse on the virtual reality track (black) with superimposed spikes during right (blue circles) and left (red circles) runs is shown at the bottom. Two firing fields were crossed twice in opposite directions. (**b**) Firing rate (top), subthreshold membrane potential (middle) and MPO_θ amplitude (bottom) indicated by dashed lines in **a** were plotted against position in the firing field (black horizontal bar). (**c**) Mouse speed (top), membrane potential of another stellate cell (middle) and MPO_θ amplitude (bottom) during a firing field crossing. (**d**) Firing rate (top), subthreshold membrane potential (middle, after removal of action potentials) and MPO_θ amplitude changes (bottom) of the stellate cell shown in **c** were plotted against the position of the mouse. R, reward points. The field crossing shown in **c** is indicated by a horizontal gray bar. (**e**) The phases of action potentials (APs) with respect to LFP theta (left), MPO_θ with respect to LFP theta (middle) and action potentials with respect to MPO_θ (right) were plotted as a function of normalized position within a firing field. (**f**) Average firing rate (top), subthreshold membrane potential (middle) and MPO_θ amplitude (bottom) were plotted against normalized position in a firing field. Shaded areas indicate ± s.e.m.

a Oscillatory interference model

● $f_i = f_b + \beta\, \mathbf{v}\cdot\mathbf{d}_i$
● f_b

100 μm

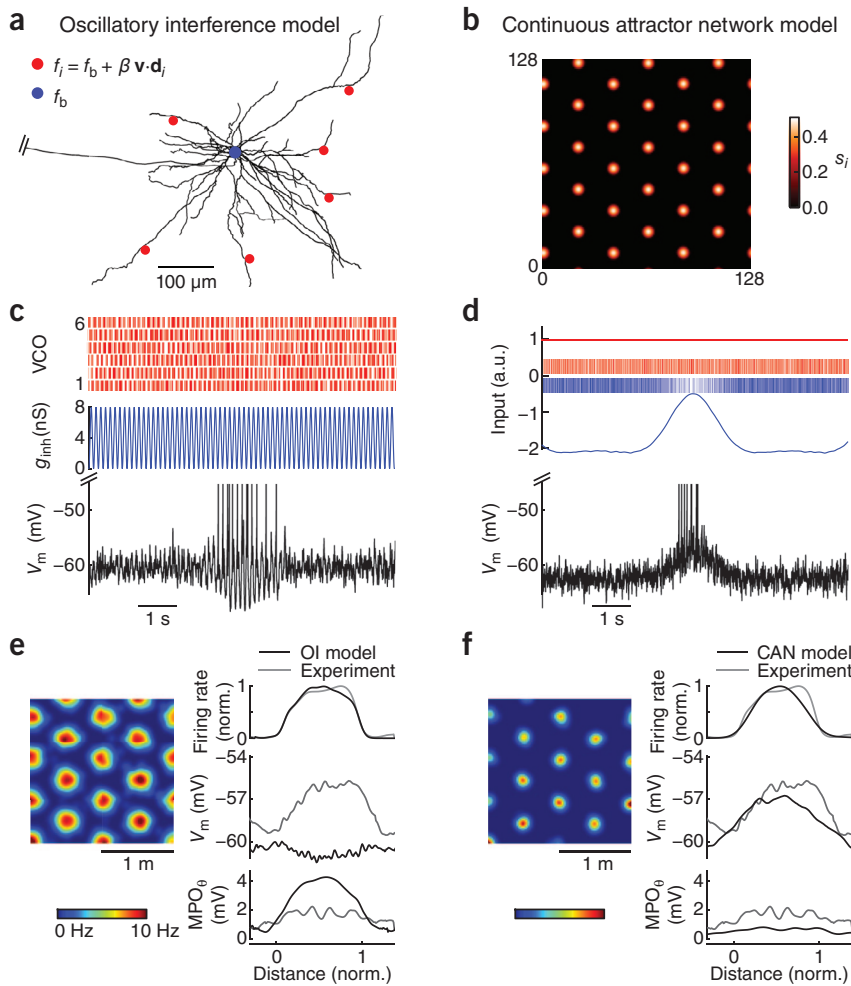**b** Continuous attractor network model

Figure 5 Comparing experimental data with grid cell models. (**a**) To implement an oscillatory interference (OI) model, six excitatory synapses (red circles) were driven by VCOs and interfered with a baseline inhibitory oscillation at the soma of a compartmental stellate cell model based on a previously described morphological reconstruction[15]. (**b**) To implement a CAN model, 128 neurons[2] were arranged on a neural sheet. Circularly symmetric center-surround connectivity led to spontaneous pattern formation of synaptic activity s_i. (**c**) Plot of VCO timings (red), inhibitory conductance oscillation (blue) and simulated membrane potential (black) in the oscillatory interference model during a field crossing. (**d**) In the CAN model, constant feedforward excitation (red trace) and recurrent inhibition (blue trace) were converted to discrete excitatory (red bars) and inhibitory (blue bars) events. The black trace shows the simulated membrane potential during a field crossing. (**e**) Left, color-coded firing rate map of the oscillatory interference model neuron. Right, average firing rate (top), subthreshold membrane potential (middle) and MPO$_\theta$ amplitude (bottom) were plotted against normalized position in a firing field. The experimental results are shown superimposed (gray). (**f**) Data are presented as in **e**, but for the CAN model.

suggest that interneurons in MEC may provide the inhibitory circuitry that is required by such a model. To obtain predictions of membrane potential dynamics during grid cell firing, we selected one of the rate-based neurons in the network and converted its synaptic input into discrete synaptic excitatory and inhibitory events that were then used to drive grid cell firing in our compartmental stellate cell model. Consistent with our experimental data, the CAN model predicted sustained depolarizations during firing field crossings[11] (**Figs. 5f** and **6b**, and **Supplementary Fig. 8**), and firing rates correlated with sub-theta membrane potential changes, but not with changes in MPO$_\theta$ amplitudes (**Fig. 6a**). The model also captured the steep decrease of sustained depolarization amplitudes with increasing initial membrane potential at the entrance of a firing field that we observed experimentally (**Supplementary Fig. 8j**). Thus, the CAN model is an example of a network model of grid cell firing that can explain the experimentally observed sustained depolarization.

Firing in this model is produced by coincidence of excitatory synaptic inputs from VCOs during grid field crossings (**Fig. 5a**). Given that the membrane time constant of stellate cells *in vivo* (~5–20 ms) is much shorter than the theta period duration of VCOs (~80–150 ms) and spikes are followed by afterhyperpolarizations, membrane potential will readily reset during the reduction of synaptic activity that occurs between these coincident inputs. Accordingly, firing in this model is driven by an increase in MPO$_\theta$ amplitude rather than by a slow, sustained depolarization, which is opposite of what we observed experimentally (**Figs. 5e** and **6a**, and **Supplementary Fig. 8**). We next tested whether a modified oscillatory interference model with slower excitatory synaptic conductance changes and little spike afterhyperpolarization would better fit our data (**Supplementary Fig. 9a,c**). Although this model predicted a small sustained depolarization in the firing field center, the slow synaptic conductance changes broadened the synaptic coincidence detection window, favoring inappropriate spike generation outside of regular grid fields. Similarly, a variant of the oscillatory interference model using inhibitory VCOs[22,23] also failed to reproduce our experimental findings (**Supplementary Fig. 9b,d**).

As an example of a network model of grid cell firing, we tested another class of grid cell firing models that builds on recurrent synaptic connectivity in a CAN of neurons[6,12] (**Fig. 5b,d,f**). We implemented a standard CAN model with purely inhibitory recurrent connectivity[12]. Recent *in vitro* studies showing that stellate cells are mostly interconnected disynaptically via inhibitory interneurons[24,25] and our own *in vivo* recordings from fast-spiking neurons (**Supplementary Fig. 3e,f**).

A hybrid model captures both the rate and temporal code

The theta phase precession that we observed is not inherently predicted by a default CAN model, which is not based on an oscillatory temporal structure. Our data suggest that stellate cells receive extrinsic theta-modulated synaptic input during locomotion (**Fig. 3**). We therefore examined whether phase precession could be produced when such theta-modulated inputs are added to the CAN model (**Fig. 7**). One possibility is that the sustained depolarizing ramp that we observed during field crossings allows the MPO$_\theta$ to exceed firing threshold successively earlier with each theta cycle, as was previously suggested as a mechanism for phase precession in place cells[26]. However, in contrast with what we observed experimentally (**Fig. 4e**), such a model predicts that action potentials will show phase precession with respect to both LFP and MPO$_\theta$ (**Fig. 7a,c,e**)[27].

Given that phase precession of both spikes and MPOs with respect to LFP are an innate property of oscillatory interference models[8,27],

Figure 6 The spiking mechanism in stellate cells is compatible with a CAN model of grid cell firing. (**a**) Normalized firing rates, as determined from the inverse of the interspike interval, were plotted against deviations of MPO_θ amplitudes (left) and sub-theta membrane potential (right) from the mean. Top, oscillatory interference model; middle, CAN model; bottom, experimental data ($n = 5$ stellate cells with firing fields). (**b**) Bar graphs summarizing maximal changes in membrane potential (top left), MPO_θ amplitudes (top right), membrane potential theta power (bottom left), and ratio of maximal changes in MPO_θ amplitude and maximal changes in membrane potential in the center of firing fields (bottom right). Changes were measured as the difference between the maximal value in the center (0.6 times the field width) of a firing field and the mean value preceding a firing field crossing over a distance of 0.6 times the field width (maximum ΔV_m: oscillatory interference, 0.9 ± 0.1 mV, mean ± s.e.m. ($n = 17$ fields); CAN, 4.0 ± 0.2 mV ($n = 18$ fields); experiment, 5.0 ± 1.0 mV ($n = 14$ fields from 6 stellate cells); maximum ΔMPO_θ: oscillatory interference, 4.1 ± 0.3 mV; CAN, 0.9 ± 0.1 mV; experiment, 2.0 ± 0.2 mV; maximum Δ theta power: oscillatory interference, 50 ± 5%; CAN, 25 ± 5%; experiment, 29 ± 5%; maximum ΔMPO_θ/maximum ΔV_m: oscillatory interference, 5.6 ± 0.9; CAN, 0.2 ± 0.0; experiment, 0.8 ± 0.3). Error bars denote s.e.m.
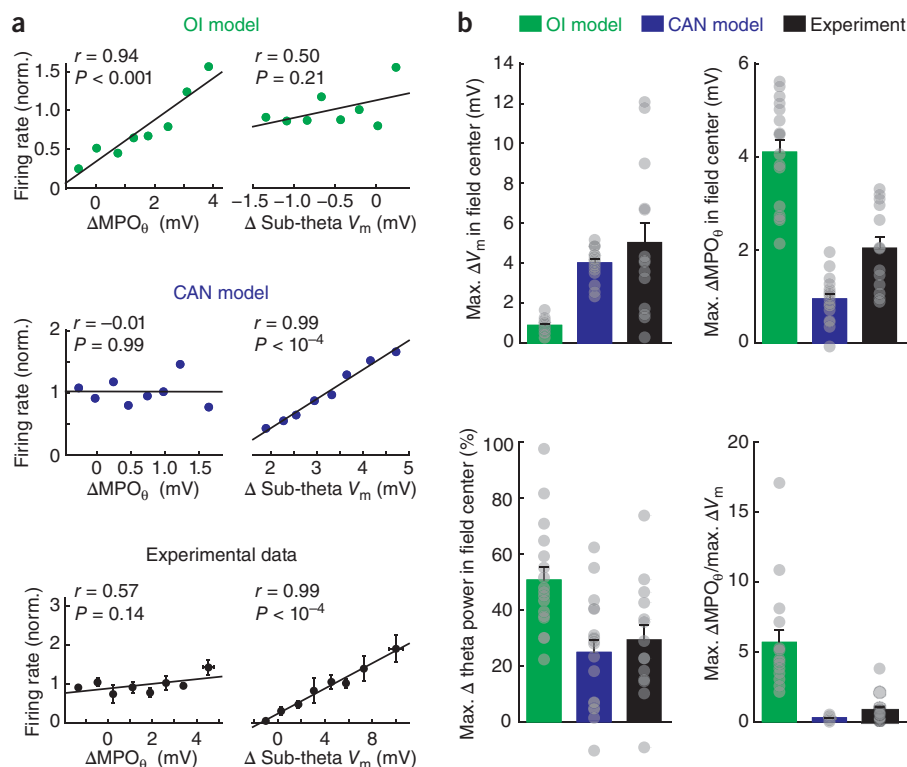
we developed a hybrid model in which VCOs provided excitatory feed-forward input to the CAN model cell. Consistent with our experimental data, this hybrid CAN and oscillatory interference model produced phase precession of action potentials with reference to the LFP, but not with respect to MPO_θ (**Fig. 7b,d,f**). There are other models that could also be consistent with our data on phase precession; for example, a CAN model was recently proposed in which phase precession is produced by the interaction between synaptic connectivity and afterspike membrane potential dynamics of stellate cells[11].

DISCUSSION

Our experiments provide, to the best of our knowledge, the first direct intracellular recordings of membrane potential in MEC neurons of navigating mice. By measuring subthreshold membrane potential, these recordings reveal how synaptic input interacts with the intrinsic properties of stellate cells to drive grid-like firing during spatial navigation. The resulting distinctive input-output signature provides crucial new information for discriminating between different models of grid cell firing. Direct comparison of our experimental data with various classes of grid cell models revealed that our results are best reproduced by models that slowly integrate synaptic inputs across several theta cycles during firing field crossings. One well-established example of a class of network models that can explain the resulting voltage ramp is the CAN model of grid cell firing. In contrast, oscillatory interference models, which rely on more rapid coincidence of VCO phases in a theta cycle, do not produce sustained depolarizations in firing fields, but can reproduce the experimentally observed phase precession. Our findings therefore provide essential constraints for any quantitative model of grid cell firing. The similarity of the membrane potential signatures in firing fields of entorhinal cortex stellate cells and hippocampal CA1 pyramidal cells[14] argues in favor of conserved synaptic mechanisms for spatially selective firing.

Our intracellular recordings revealed that theta oscillations appear in subthreshold membrane potential during movement specifically in stellate cells. This is consistent with observations made during LFP theta periods in anesthetized animals[21]. Given that sustained depolarization failed to evoke membrane potential oscillations in stellate cells *in vivo*, it seems likely that the oscillations during movement are caused by direct or indirect inputs from neurons that exhibit locomotion-dependent theta modulation of action potential firing, such as inputs to entorhinal cortex from medial septum that are known to affect grid cell firing[28,29]. Why is theta periodicity of membrane potential much less pronounced in pyramidal neurons of MEC? Stellate cells, in contrast with pyramidal cells, show pronounced resonance in the theta frequency range *in vitro*[30]. This resonance could selectively amplify theta-modulated synaptic inputs that are shared between stellate and pyramidal cells. Alternatively, theta-modulated synaptic inputs might specifically target stellate cells. Voltage-clamp experiments in navigating animals will help to distinguish between these scenarios.

We found that, in stellate cells, the transition to firing when entering a firing field is driven by a slow depolarization of membrane potential, with only little increase in MPO_θ amplitude. This signature closely matches grid cell models that predict a sustained, continuous increase in net excitatory drive when animals move toward the center of a firing field, such as, for example, the CAN model[6,12]. Future experiments recording the activity of a large population of identified neurons will be required to determine which sources of excitatory and inhibitory synaptic inputs to grid cells drive this shift in excitation-inhibition balance, and to distinguish between CAN and other models that can potentially produce slow synaptic integration processes during firing field crossings[31,32].

In contrast, the default oscillatory interference model based on temporal interference of VCOs in the theta frequency band neither predicts nor requires the sustained depolarizations that we observed during firing field crossings. In this model, net excitation per theta

Figure 7 Rate and temporal code of grid cell firing are reproduced by a hybrid CAN and oscillatory interference model. We constructed two variants of the standard CAN model to produce phase precession. (**a,c,e**) In the first variant, we combined a CAN model with additional slow recurrent inhibition to generate a depolarizing voltage ramp. Excitation (red trace) and inhibition (blue trace) were converted to discrete inhibitory (blue bars) and theta-modulated excitatory (red bars) events (**a**). The black trace shows the simulated membrane potential during a firing field crossing. (**c**) Left, color-coded firing rate map of the model neuron. Right, average firing rate (top), subthreshold membrane potential (middle) and MPO_θ amplitudes (bottom) were plotted against normalized position in a firing field. The experimental results are shown superimposed (gray). (**e**) The phase of spikes with reference to the LFP theta (left), subthreshold membrane potential oscillations with reference to the LFP theta (middle) and spikes with reference to the MPO_θ were plotted as a function of normalized position in a firing field. Phase precession slope for spikes with reference to the LFP theta ($-86°$ per field, $r = -0.59$, $P < 10^{-4}$). Phase precession for MPOs with reference to the LFP theta ($-5°$ per field, $r = -0.11$, $P = 0.50$). Phase precession for spikes with reference to MPO_θ ($-73°$ per field, $r = -0.49$, $P < 0.0005$). (**b,d,f**) In the second variant, we combined a CAN with an oscillatory interference model. In this hybrid model, feedforward excitatory events were provided by two VCOs (red bars) (**b**). Recurrent inhibition (blue trace) was converted to discrete inhibitory events (blue bars). The black trace shows the simulated membrane potential during a firing field crossing. (**d**) Data are presented as in **c** for the hybrid model. (**f**) Data are presented as in **e** for the hybrid model. Phase precession slope for spikes with reference to the LFP theta ($-144°$ per field, $r = -0.50$, $P < 10^{-4}$). Phase precession for MPOs with reference to the LFP theta ($-136°$ per field, $r = -0.84$, $P < 10^{-4}$). Phase precession for spikes with reference to MPO_θ ($-11°$ per field, $r = -0.05$, $P = 0.39$).
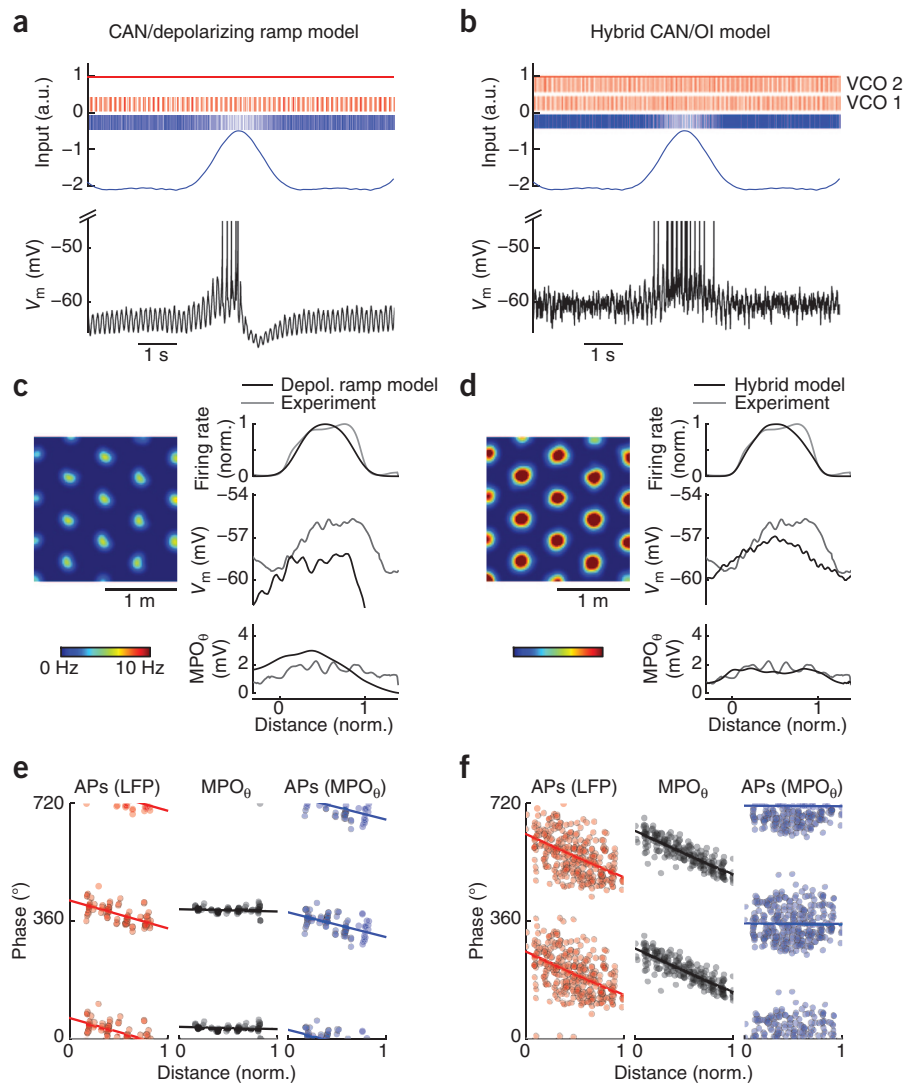
cycle is the same inside and outside the firing fields at a given animal velocity because the frequency of each individual VCO is constant, with firing being produced by rapid coincidence of VCO phases in theta periods. It is possible to engineer interference model variants that produce sustained depolarization during firing field crossings. For example, a model with very low VCO frequencies or spatial interference models could produce sustained depolarizations. However, interference models with VCO frequencies well below the theta range lose their innate ability to produce theta phase precession, which was the original motivation to develop this class of models[33]. Indeed, the experimentally observed phase precession of both spikes and MPOs with respect to LFP theta is perfectly predicted by the default oscillatory interference model.

CAN and oscillatory interference models are not mutually exclusive[8,34], and we found that a hybrid model can explain both the rate and the temporal code of the experimentally observed firing of putative grid cells. In the hybrid model, theta-modulated VCOs, or the asymmetric connections of the CAN model with an additional layer of velocity-sensitive neurons[4], could provide the path integration mechanism by coupling the patterns of neural activity to the movement of the animal. Nonetheless, our results make it unlikely that the rate code is generated primarily by a theta-modulated mechanism; however, the temporal code (at least in rodents; see ref. 35) is consistent with predictions from an oscillatory interference model. In summary, although future experiments probing the anatomical connectivity and population firing patterns of the MEC network will also be required, our experimental data provide crucial clues to the mechanisms that create grid cells.

METHODS

Methods and any associated references are available in the online version of the paper.

Note: Supplementary information is available in the online version of the paper.

AUTHOR CONTRIBUTIONS

C.S.-H. and M.H. designed the study, interpreted the results and wrote the paper. C.S.-H. performed the experiments, analysis and modeling.

COMPETING FINANCIAL INTERESTS

The authors declare no competing financial interests.

Reprints and permissions information is available online at http://www.nature.com/reprints/index.html.

1. Hafting, T., Fyhn, M., Molden, S., Moser, M.B. & Moser, E.I. Microstructure of a spatial map in the entorhinal cortex. *Nature* **436**, 801–806 (2005).
2. Sargolini, F. *et al.* Conjunctive representation of position, direction, and velocity in entorhinal cortex. *Science* **312**, 758–762 (2006).
3. Fyhn, M., Hafting, T., Witter, M.P., Moser, E.I. & Moser, M.B. Grid cells in mice. *Hippocampus* **18**, 1230–1238 (2008).
4. Hafting, T., Fyhn, M., Bonnevie, T., Moser, M.B. & Moser, E.I. Hippocampus-independent phase precession in entorhinal grid cells. *Nature* **453**, 1248–1252 (2008).
5. Reifenstein, E.T., Kempter, R., Schreiber, S., Stemmler, M.B. & Herz, A.V. Grid cells in rat entorhinal cortex encode physical space with independent firing fields and phase precession at the single-trial level. *Proc. Natl. Acad. Sci. USA* **109**, 6301–6306 (2012).
6. Fuhs, M.C. & Touretzky, D.S. A spin glass model of path integration in rat medial entorhinal cortex. *J. Neurosci.* **26**, 4266–4276 (2006).
7. McNaughton, B.L., Battaglia, F.P., Jensen, O., Moser, E.I. & Moser, M.B. Path integration and the neural basis of the 'cognitive map'. *Nat. Rev. Neurosci.* **7**, 663–678 (2006).
8. Burgess, N. Grid cells and theta as oscillatory interference: theory and predictions. *Hippocampus* **18**, 1157–1174 (2008).
9. Burgess, N., Barry, C. & O'Keefe, J. An oscillatory interference model of grid cell firing. *Hippocampus* **17**, 801–812 (2007).
10. Hasselmo, M.E., Giocomo, L.M. & Zilli, E.A. Grid cell firing may arise from interference of theta frequency membrane potential oscillations in single neurons. *Hippocampus* **17**, 1252–1271 (2007).
11. Navratilova, Z., Giocomo, L.M., Fellous, J.-M., Hasselmo, M.E. & McNaughton, B.L. Phase precession and variable spatial scaling in a periodic attractor map model of medial entorhinal grid cells with realistic after-spike dynamics. *Hippocampus* **22**, 772–789 (2012).
12. Burak, Y. & Fiete, I.R. Accurate path integration in continuous attractor network models of grid cells. *PLoS Comput. Biol.* **5**, e1000291 (2009).
13. Hölscher, C., Schnee, A., Dahmen, H., Setia, L. & Mallot, H.A. Rats are able to navigate in virtual environments. *J. Exp. Biol.* **208**, 561–569 (2005).
14. Harvey, C.D., Collman, F., Dombeck, D.A. & Tank, D.W. Intracellular dynamics of hippocampal place cells during virtual navigation. *Nature* **461**, 941–946 (2009).
15. Brun, V.H. *et al.* Progressive increase in grid scale from dorsal to ventral medial entorhinal cortex. *Hippocampus* **18**, 1200–1212 (2008).
16. Alonso, A. & Klink, R. Differential electroresponsiveness of stellate and pyramidal-like cells of medial entorhinal cortex layer II. *J. Neurophysiol.* **70**, 128–143 (1993).
17. Garden, D.L., Dodson, P.D., O'Donnell, C., White, M.D. & Nolan, M.F. Tuning of synaptic integration in the medial entorhinal cortex to the organization of grid cell firing fields. *Neuron* **60**, 875–889 (2008).
18. Giocomo, L.M., Zilli, E.A., Fransén, E. & Hasselmo, M.E. Temporal frequency of subthreshold oscillations scales with entorhinal grid cell field spacing. *Science* **315**, 1719–1722 (2007).
19. Fernandez, F.R. & White, J.A. Artificial synaptic conductances reduce subthreshold oscillations and periodic firing in stellate cells of the entorhinal cortex. *J. Neurosci.* **28**, 3790–3803 (2008).
20. Nolan, M.F., Dudman, J.T., Dodson, P.D. & Santoro, B. HCN1 channels control resting and active integrative properties of stellate cells from layer II of the entorhinal cortex. *J. Neurosci.* **27**, 12440–12451 (2007).
21. Quilichini, P., Sirota, A. & Buzsáki, G. Intrinsic circuit organization and theta-gamma oscillation dynamics in the entorhinal cortex of the rat. *J. Neurosci.* **30**, 11128–11142 (2010).
22. Welday, A.C., Shlifer, I.G., Bloom, M.L., Zhang, K. & Blair, H.T. Cosine directional tuning of theta cell burst frequencies: evidence for spatial coding by oscillatory interference. *J. Neurosci.* **31**, 16157–16176 (2011).
23. Zilli, E.A. & Hasselmo, M.E. Coupled noisy spiking neurons as velocity-controlled oscillators in a model of grid cell spatial firing. *J. Neurosci.* **30**, 13850–13860 (2010).
24. Pastoll, H., Solanka, L., van Rossum, M.C. & Nolan, M.F. Feedback inhibition enables theta-nested gamma oscillations and grid firing fields. *Neuron* **77**, 141–154 (2013).
25. Couey, J.J. *et al.* Recurrent inhibitory circuitry as a mechanism for grid formation. *Nat. Neurosci.* 10.1038/nn.3310 (2013).
26. Mehta, M.R., Lee, A.K. & Wilson, M.A. Role of experience and oscillations in transforming a rate code into a temporal code. *Nature* **417**, 741–746 (2002).
27. Burgess, N. & O'Keefe, J. Models of place and grid cell firing and theta rhythmicity. *Curr. Opin. Neurobiol.* **21**, 734–744 (2011).
28. Koenig, J., Linder, A.N., Leutgeb, J.K. & Leutgeb, S. The spatial periodicity of grid cells is not sustained during reduced theta oscillations. *Science* **332**, 592–595 (2011).
29. Brandon, M.P. *et al.* Reduction of theta rhythm dissociates grid cell spatial periodicity from directional tuning. *Science* **332**, 595–599 (2011).
30. Haas, J.S. & White, J.A. Frequency selectivity of layer II stellate cells in the medial entorhinal cortex. *J. Neurophysiol.* **88**, 2422–2429 (2002).
31. Kropff, E. & Treves, A. The emergence of grid cells: intelligent design or just adaptation? *Hippocampus* **18**, 1256–1269 (2008).
32. Zilli, E.A. Models of grid cell spatial firing published 2005–2011. *Front. Neural Circuits* **6**, 16 (2012).
33. O'Keefe, J. & Recce, M.L. Phase relationship between hippocampal place units and the EEG theta rhythm. *Hippocampus* **3**, 317–330 (1993).
34. Hasselmo, M.E. & Brandon, M.P. A model combining oscillations and attractor dynamics for generation of grid cell firing. *Front. Neural Circuits* **6**, 30 (2012).
35. Yartsev, M.M., Witter, M.P. & Ulanovsky, N. Grid cells without theta oscillations in the entorhinal cortex of bats. *Nature* **479**, 103–107 (2011).
36. Dodson, P.D., Pastoll, H. & Nolan, M.F. Dorsal-ventral organization of theta-like activity intrinsic to entorhinal stellate neurons is mediated by differences in stochastic current fluctuations. *J. Physiol. (Lond.)* **589**, 2993–3008 (2011).

ONLINE METHODS

Surgical procedures. All experiments were carried out in accordance with UK Home Office regulations. Adult C57BL/6J male mice (6–12 weeks old) were anesthetized with isoflurane (5% for induction, 1–3% for surgery, vol/vol). Stainless steel headposts were cemented to the mouse skull using dental acrylic. Craniotomies were drilled for the recording pipette (right hemisphere, 3.2–3.5 mm lateral from lambda, midway between lambdoid suture and transverse sinus, 0.5-mm diameter) and the reference electrode (0.2–0.3-mm diameter) 6–48 h before recordings.

Virtual-reality environment. A custom virtual-reality environment was developed, integrating an air-supported polystyrene ball that served as a spherical treadmill for head-restrained mice[13,14]. A quarter-sphere mirror (45-cm diameter) placed underneath the mouse reflected the projected warped image onto a spherical dome screen (120-cm diameter)[37]. The screen covered 240°, that is, nearly the entire horizontal field of view of the mouse[38]. All of the projection apparatus, including the WXGA LCD projector (NEC NP510W), was located below the mouse, allowing an unobstructed field of view and ready access for the electrophysiological recording assembly. Ball rotations associated with mouse locomotion were read out with two computer mice (Logitech G500) at the anterior and left poles of the ball at a poll rate of 1 kHz and linearly converted to a movement in a rectangular virtual reality scene. Ball rotations around the mediolateral axis were used for forward and backward movement along the running direction of the mouse, whereas ball rotations around the anteroposterior and dorsoventral axes were used in combination to change the mouse's running direction. Whereas head fixation would likely interfere with the head-direction system, we decided to use a three-dimensional environment instead of a purely linear track to preserve a more realistic directional input as much as possible by allowing the mouse to freely choose its running direction. For intracellular recordings, the environment was 0.27 m wide and 4.3 m long. For extracellular recordings, the environment was restricted to a width of 0.14 m and a length of 2.24 m to favor multiple field crossings (**Supplementary Fig. 1c**). The Blender Game Engine (http://www.blender.org) was used in conjunction with the Blender Python API to drive the virtual reality system.

Behavioral training. Mice underwent 5–10 training sessions, ~1 h each, over the course of 1–2 weeks before recordings (**Fig. 1c**). Mice were neither food- nor fluid-deprived at any time and housed in a regular light/dark cycle with four mice per cage. Training and recordings were performed during the light cycle of the mice. To increase recording stability by reducing lateral movement of the body against the head, we placed a harness around the mouse's thorax during training and recording. Air puffs were applied to the whiskers whenever the mouse touched a boundary in the virtual environment. Rewards (80 mg ml^{−1} sugar water) were delivered to increase the motivation of the mouse to explore the environment. Five reward points were distributed along the track with a spacing of 0.96 m. Only one of the reward points was active and visible to the mouse at any time. Whenever the mouse reached one of the reward points, the reward point disappeared and became inactive, an acoustic signal sounded, 10 µl of sugar water was dispensed and the next reward point along the track was activated. Reward activation direction was reversed to motivate the mouse to turn around when it had emptied one of the reward points at either end of the track.

Electrophysiology. Whole-cell patch-clamp recordings were obtained using glass pipettes pulled from borosilicate glass (~5-MΩ pipette resistance) and filled with internal solution containing 135 mM potassium methanesulphonate, 10 mM HEPES, 1 mM sodium phosphocreatine, 7.4 mM KCl, 0.3 mM MgCl$_2$, 0.1 mM EGTA, 3.0 mM Na$_2$ATP, 0.3 mM NaGTP and 5 mg ml^{−1} biocytin, pH 7.2. In some recordings, a tungsten electrode (~1-MΩ resistance) was lowered into the brain along with the patch pipette to record the LFP simultaneously. The distance between the patch pipette and tungsten electrode tips was <100 µm. Pipettes were lowered into the dorsal part of the medial entorhinal cortex to a depth of ~1.5–2.2 mm measured from the dorsal surface of the brain at an angle of 6° in the anterior-to-posterior direction in the sagittal plane[3] (**Supplementary Fig. 1a**). Whole-cell patch-clamp recordings were obtained using a standard blind-patch approach[39]. Seal resistances were always ≫1 GΩ, and access resistances were typically 25–70 MΩ, with recordings terminated when access resistance exceeded 100 MΩ. Recordings were made in current-clamp mode, and no

holding current was applied during mouse navigation (**Figs. 3** and **4**). Typical recording durations were ~5 min (which usually allowed mice to cross firing fields only once during the recording), although longer recordings (~30 min) were occasionally achieved. Extracellular unit recordings in **Supplementary Figure 1b,c** were obtained with a patch pipette before approaching neurons for whole-cell recordings or following unsuccessful whole-cell recording attempts. Membrane potential and LFP signals were low-pass filtered at 10 kHz and 1 kHz, respectively, and acquired at 50 kHz.

Immunohistochemistry and cell identification. At the end of some recordings, mice were deeply anesthetized with an overdose of ketamine (intraperitoneal) and quickly perfused transcardially with 0.1 M phosphate-buffered saline followed by a 40 mg ml^{−1} paraformaldehyde solution. Brains were removed from the skull and kept in paraformaldehyde for at least 24 h. We stained 80-µm-thick parasagittal slices with Alexa Fluor 488–streptavidin to reveal biocytin-filled neurons and patch pipette tracts.

We made whole-cell patch-clamp recordings from a total of 177 neurons in MEC. Of these, 26 neurons were identified as layer II stellate cells by their characteristic electrophysiological signature, including the presence of sag during hyperpolarizing voltage responses (sag ratio = 0.61 ± 0.01, range = 0.50–0.73), biphasic afterhyperpolarizations following action potentials, and little adaptation during spike trains[16,17,21]. The identity of eight stellate neurons was also confirmed morphologically following biocytin staining and processing[40]. In addition, the pipette tract was confirmed to terminate in layer II of MEC in a further eight stellate cell recordings in which morphological processing was performed, but the morphology of the biocytin-labeled neuron could not be recovered. Sixteen stellate cell recordings included enough resting periods to measure spontaneous firing rates as described below. In 15 stellate cell recordings, membrane potential was depolarized close to spike threshold for ≥1 s by sustained current injections in resting mice so that we could assess theta periodicity as described below. Eight stellate cell recordings that included more than 30 s of movement episodes (mouse speed ≥ 0.5 cm s^{−1}) were used to assess membrane potential dynamics during virtual navigation (recording duration used for analysis = 265 ± 50 s, *n* = 8). In two of these recordings, cells fired either no spikes (**Supplementary Fig. 2d–h**) or only few spikes during movement. The six remaining stellate cells showed distinct firing fields (**Supplementary Fig. 7**). Five of these recordings during which the LFP was simultaneously recorded were used to assess phase precession (**Fig. 4e** and **Supplementary Fig. 6**).

Some recordings were obtained from a distinct subset of fast-spiking putative interneurons in layers II/III of MEC exhibiting rapid, monophasic spike afterhyperpolarizations (*n* = 7; **Supplementary Fig. 3**). In these neurons, spike rates following depolarization exceeded 100 Hz and lacked spike adaptation (173 ± 28 Hz, range = 102–297 Hz). A further set of neurons (*n* = 111 neurons) exhibited properties reminiscent of pyramidal cells, with no noticeable sag in response to small hyperpolarizing sustained current injections, no fast hyperpolarization following action potentials, and no non-adapting fast spike trains. Indeed, when morphological recovery of their morphology was possible, two of these neurons were identified as layer V pyramidal cells, four as layer II/III pyramidal cells, and, in an additional three recordings, the pipette tract terminated in layers II/III (**Supplementary Fig. 4**). Basic electrophysiological properties were not significantly different between the 105 unstained neurons and the six confirmed pyramidal neurons (*P* > 0.4 for all tested properties; **Supplementary Fig. 4d–f**). Because an unambiguous classification based on electrophysiology alone was not possible, we categorized this whole set of recordings as putative pyramidal cells. We cannot rule out the possibility that a small fraction of these neurons may represent non–fast-spiking interneurons or non-pyramidal principal neurons from deeper layers of MEC. Finally, 33 neurons could not be reliably classified as stellate, fast-spiking or pyramidal cells. In some of these neurons, strong spontaneous synaptic activity made it impossible to clearly assess voltage sag and action potential shape for a purely electrophysiological characterization. Another part of this population produced two or less spikes during sustained current injections or showed input resistances >300 MΩ. We did not use these cells for analysis.

Several lines of evidence suggest that the stellate cells we recorded from are grid cells. First, our extracellular unit recordings from layer II of MEC revealed multiple firing fields that were reproducible during repeated runs (**Supplementary Fig. 1b,c**), consistent with grid cell firing on a linear track[15].

Second, we observed phase precession during firing field crossings (**Fig. 4e**), which has been shown to provide strong and robust encoding of physical space[4,5]. Third, in a stellate cell in which it was possible to maintain the recording during a prolonged linear run, the cell exhibited a markedly periodic pattern of five firing fields (**Fig. 4d**). Fourth, firing was reproducible during repeated runs through two firing fields in another recording (**Fig. 4a** and **Supplementary Fig. 7**). Fifth, firing fields did not arise as a simple consequence of mouse speed changes (**Supplementary Fig. 10**). Finally, our recordings focused on stellate cells in layer II of MEC, where most pure grid cells are found[2]. It is therefore unlikely that firing could be generated by head direction, boundaries or contextual cues. We also note that all firing fields in all stellate cells were accompanied by sustained increases in membrane potential (**Supplementary Figs. 7** and **8**), suggesting that the general firing mechanism in these neurons is inconsistent with the rapid coincidence detection in theta cycles predicted by the oscillatory interference model.

Data analysis. Input resistance was calculated from the steady-state voltage response to a small hyperpolarizing 1-s current pulse from resting membrane potential. Sag ratio was measured as the ratio of the steady state and the peak voltage responses to this current pulse (**Fig. 1e** and **Supplementary Fig. 2a–c**). Only data from mice that were resting during this period were used. Resting membrane potential was measured as the membrane potential baseline during a period of low synaptic activity in mice at rest at the beginning of the recording. Spontaneous firing rate was measured across multiple resting periods using only recordings in which the mouse rested (mouse speed < 0.5 cm s^{-1}) during more than 5 s. Extracellular spikes (**Supplementary Fig. 1b,c**) were detected by first high-pass filtering ($f_c = 0.2$ kHz) and then thresholding the extracellular voltage trace. Spikes were then sorted using principal component analysis. Clusters representing unitary spikes were manually selected using the first three principal components. Analysis was restricted to the recording period between the first and the last detected spikes.

To analyze subthreshold membrane potential, traces were digitally low-pass filtered at 5 kHz and resampled at 10 kHz. In some cases, we corrected for a linear drift of baseline membrane potential (<5 mV over 10 min) that was presumably caused by a drift in the reference potential. Action potentials were then removed by thresholding to determine action potential times and then replacing 2 ms before and 10–20 ms after the action potential peak (depending on action potential shape) with an interpolated straight line. Membrane potential oscillations in the theta frequency range (MPO$_\theta$) were analyzed by bandpass-filtering membrane potential traces (5–10 Hz) after removal of action potentials. To quantify the MPO$_\theta$ amplitude, we computed the envelope of the bandpassed membrane potential using the absolute value of the Hilbert transform (**Supplementary Fig. 6b**). Power spectra were computed from subthreshold membrane potential traces or LFP traces using Hanning windowing over data windows of 2^{15} sampling points (~328 ms). To obtain spectrograms in **Figure 3e**, we first computed average spectrograms aligned to the onset of running for each cell (running duration > 3 s, mean speed + s.d. during a 5-s resting period was used as threshold for the onset of running). We then normalized each average spectrogram of a cell to its maximal value before computing the average across cells. Resting and running power spectra in **Figure 3f** and **Supplementary Fig. 5d,f** were obtained 2 s before and 2 s after the onset of running, respectively. To assess the significance of peaks in the theta band of the power spectrum, membrane potential traces were low-pass filtered at 50 Hz and resampled at 100 Hz. We then used the Lomb-Scargle method with an oversampling factor of 4 to detect peaks at a significance value of 0.01 (**Supplementary Fig. 5c**)[36].

To generate firing rate and membrane potential maps of experimental and simulated data (for example, **Fig. 4f**), we used a spatial smoothing algorithm[1]. The firing rate λ at any position x along the long axis of the track was computed as

$$\lambda(x) = \frac{\sum_{i=1}^{n} g\left(\dfrac{s_i - x}{h_\lambda}\right)}{\int_0^T g\left(\dfrac{y(t) - x}{h_\lambda}\right) dt} \qquad (1)$$

where g is a filter kernel ($g(x) = e^{-x}$), $h_\lambda = 3$ cm, s_i is the location of the ith spike, $y(t)$ is the location of the mouse at time t along the long axis of the track, and T is the recording duration. Subthreshold membrane potential V_m, MPO$_\theta$ and theta power of V_m at any position x along the long axis of the track were computed as

$$V(x) = \frac{\sum_{i=1}^{n} v_i g\left(\dfrac{p_i - x}{h_V}\right)}{\sum_{i=1}^{n} g\left(\dfrac{p_i - x}{h_V}\right)} \qquad (2)$$

where $h_V = 1$ cm, v_i is the ith recorded data sample (sampled at equal intervals in time), p_i is the location where v_i was recorded along the long axis of the track, and n is the number of membrane potential sampling points. Maps were discretized into bins with a spacing of 0.5 cm along the long axis of the track. Each bin covered the full extent of the short axis of the track. All spatial maps of V_m, MPO$_\theta$ and theta power of V_m were generated using this procedure. An additional set of spatial maps was computed for V_m with $h_V = 0.2$ cm and a bin spacing of 0.1 cm (**Supplementary Fig. 8d–f**) to assess the effects of spatiotemporal filtering. V_m, MPO$_\theta$ and theta power of V_m at the entry of a firing field (V_0) were computed as the mean value of $V(x)$ preceding a firing field crossing over a distance of 0.6 times the field width. ΔV_m, ΔMPO$_\theta$ and Δtheta power of V_m were computed as $V(x) - V_0$.

Unless stated otherwise, only data from periods during which the mouse ran faster than 5 cm s^{-1} were used to detect and analyze spatial firing fields. To isolate running periods, speed traces were low-pass filtered at 10 Hz. A firing field was estimated as a contiguous region of at least 16 bins where the firing rate was above 20% of the peak rate of a cell's spatial firing map. Fields with peak rates <1Hz were discarded. To compute averages of multiple spatial firing fields across cells (for example, **Fig. 4f**), positions in a field were aligned and normalized so that 0 corresponded to field entry and 1 corresponded to field exit along the long axis of the track. When fields were crossed multiple times (**Fig. 4a** and **Supplementary Fig. 7**), we first aligned and normalized field crossings individually and then computed the average of all crossings for each field before computing the average across fields.

To assess phase precession of MPO$_\theta$ and spike firing, we aligned and normalized 12 fields from 5 stellate cells in which an LFP recording was available as described above. Slope, phase offset, correlation coefficients and significance of phase precession (**Figs. 4e** and **7e,f**) were quantified using a circular-linear approach[41]. 0° denotes peaks of the LFP theta wave.

To generate firing rate dependency plots (**Fig. 6a**), we computed sub-theta membrane potential by bandpass-filtering of membrane potential between 0.1 and 5 Hz after removing action potentials and subtracting the mean. Changes in sub-theta membrane potential (Δsub-theta V_m) and in MPO$_\theta$ amplitudes (ΔMPO$_\theta$) were measured as deviations from the mean of each cell. Firing rates were computed as the inverse of the interspike interval (ISI) and normalized to the mean firing rate of each cell. For each ISI, we computed the corresponding mean value of Δsub-theta V_m or Δ MPO$_\theta$ during the ISI. For each cell, average firing rates and corresponding average Δsub-theta V_m or ΔMPO$_\theta$ values were computed within eight bins covering the range of measured values of Δsub-theta V_m or ΔMPO$_\theta$ before averaging across cells. Only data obtained during running periods (mouse speed > 5 cm s^{-1}) from $n = 5$ stellate cells with firing fields and a minimal interspike interval < 250 ms were used.

Statistical significance was assessed using a two-sided Mann-Whitney U test for unpaired data and a two-sided Wilcoxon signed-rank test for paired data. Data are presented as mean ± s.e.m.

Modeling. For detailed compartmental modeling with NEURON[42], we used a previously described reconstructed morphology of a mouse MEC stellate cell[17]. Hyperpolarization-activated cyclic nucleotide–gated (HCN) channel gating kinetics and densities were adopted from a previously described stellate cell compartmental model[43]. Voltage-gated potassium and sodium channel kinetics were adopted from a CA1 pyramidal cell model[44] and adjusted to match our experimental data from stellate cell recordings in awake mice (**Supplementary Table 1**). Axial resistivity was set to 139 Ω cm. Specific membrane resistance R_m and capacitance C_m were set to 30 kΩ cm^2 and 1 μF cm^{-2}, respectively, resulting in an apparent membrane time constant of ~15 ms in the presence of HCN channels.

Grid cell firing in all models was generated by simulating 90 linear mouse runs at a speed of 0.2 m s^{-1} from the (0,0) coordinate to the opposing boundaries of the environment (a 2 × 2 m^2 square box) at angles spaced by 1° (**Figs. 5e,f** and **7c,d**, and **Supplementary Fig. 9c,d**). For all simulations, amplitudes of synaptic conductance changes were adjusted to produce a maximal firing rate of ~10 Hz during grid cell firing, minimize the occurrence of spikes outside of regular grid fields, and yielded a resting membrane potential of ~−60 mV (**Supplementary Table 1**).

An oscillatory interference model[8,9] was implemented by driving six pairs of input synapses on distal dendrites of the compartmental stellate cell model with VCOs. A sinusoidal somatic inhibitory conductance change provided a baseline oscillation with frequency f_b = 8 Hz. The burst firing frequency of a VCO with index i was computed as $f_i = f_b + \beta s \cos(\varphi - \varphi_{p,i})$, where the scaling factor β is 0.02 cm^{-1}, s is mouse speed, φ is running direction and $\varphi_{p,i} = i \cdot 60°$ is the preferred direction of VCO$_i$. For each VCO, firing probability at time t was computed as $P_i(t, t + \Delta t) = (\cos(2\pi f_i t) + 1)\Delta t / 8$. We then generated Poisson spike trains from these probabilities, choosing a small interval Δt so that $P \ll 1$ (**Fig. 5c** and **Supplementary Fig. 9a**). For an inhibitory implementation of the oscillatory interference model, probabilities were computed as $P_i(t, t + \Delta t) = (1 - \cos(2\pi f_i t))\Delta t / 8$ (**Supplementary Fig. 9b**). Parameters for compartmental modeling are summarized in **Supplementary Table 1**.

A CAN model was implemented in a sheet of 128×128 neurons with periodic boundaries as described previously[12]. To improve computational efficiency, we first used rate-based model neurons to simulate the full CAN. The inhibitory and excitatory synaptic input rates of one of the rate-based neurons were then used to drive a single compartmental model neuron to make biophysically realistic predictions of membrane potential trajectories. In brief, the dynamics of rate-based neurons was defined by

$$\tau \frac{ds_i}{dt} = f(I_i + B_i) - s_i \qquad (3)$$

with

$$I_i = \sum_j W_{ij} s_j \qquad (4)$$

where I_i is inhibitory recurrent input to neuron i, W_{ij} is the synaptic weight from neuron j to neuron i, s_i is the synaptic activation of neuron i, τ = 10 ms is the time constant of the neural response, f is a rectification function ($f(x) = x$ for $x > 0$, and 0 otherwise), and B_i is excitatory feedforward input to neuron i

$$B_i = 1 + \alpha \hat{\mathbf{e}}_{\varphi_i} \cdot \mathbf{v} \qquad (5)$$

where $\hat{\mathbf{e}}_{\varphi_i}$ is the unit vector pointing along neuron i's preferred direction φ_i (one of W, N, S, or E), $\mathbf{v}$ is the mouse velocity vector in m s^{-1}, and α was set to 0.1105. The recurrent weight matrix was purely inhibitory in our implementation[12,24,25]

$$W_{ij} = W_0(\mathbf{x}_i - \mathbf{x}_j - l\hat{\mathbf{e}}_{\varphi_i}) \qquad (6)$$

with

$$W_0(\mathbf{x}) = e^{-\gamma |\mathbf{x}|^2} - e^{-\beta |\mathbf{x}|^2} \qquad (7)$$

where $\mathbf{x}_i$ is neuron i's location in the neural sheet and ranges from $(-64, -64)$ to $(64, 64)$. In our implementation, we used $l = 2$, $\gamma = 1.05\,\beta$, $\beta = 3\lambda^{-2}$, and $\lambda = 16$. To derive predictions of membrane potential dynamics during grid cell firing, we converted the synaptic inputs I_i (equation (4)) and B_i (equation (5)) of one of the rate-based neurons in the neural sheet into probabilities of excitatory and inhibitory events according to $P_{exc}(t, t + \Delta t) = f(B_i)\Delta t$ and $P_{inh}(t, t + \Delta t) = f(-I_i)\Delta t$ (**Fig. 5d**). We then generated Poisson spike trains from these probabilities as described above for the oscillatory interference model. These events were then used to drive dendritic excitatory and somatic inhibitory synaptic conductance changes in the compartmental stellate cell model using the same active and passive parameters as for the oscillatory interference model (**Supplementary Table 1**).

We implemented a depolarizing ramp model (**Fig. 7a,c,e**) on top of the CAN model described above. Excitatory feedforward inputs were modulated at a constant LFP theta frequency f_{LFP} = 8 Hz according to $P_{exc}(t, t + \Delta t) = (\cos(2\pi f_{LFP} t) + 1)f(B_i)\Delta t$. In addition to the inhibition provided by the CAN (I_i), a slow inhibitory recurrent mechanism that was activated by action potential firing with a delay of 470 ms generated an asymmetric voltage ramp with a steep decay. Another fast recurrent inhibitory mechanism was activated by action potential firing without any delay to prevent burst firing in theta cycles (**Supplementary Table 1**).

We also implemented a hybrid CAN and oscillatory interference model (**Fig. 7b,d,f**) in which feedforward excitation was provided by two VCOs with preferred angles $\varphi_{p,i}$ at 30° and 90°. Firing probability of VCO$_i$ at time t was computed as $P_i(t, t + \Delta t) = B(t)/\max(B)\{[\cos(2\pi f_i t) + 1](1 - c)/2 + c\}\Delta t$, where $B(t)$ is feed-forward input at time t in the CAN model (equation (5)), $\max(B)$ is the maximal value of B throughout all simulated mouse runs, and $c = 1/4$ is a fraction of feedforward excitation that remains unmodulated by theta. Poisson spike trains were generated as described for the oscillatory interference model.

37. Bourke, P. Spherical mirror: a new approach to hemispherical dome projection. *Planetarian* **34**, 6–9 (2005).
38. Wagor, E., Mangini, N.J. & Pearlman, A.L. Retinotopic organization of striate and extrastriate visual cortex in the mouse. *J. Comp. Neurol.* **193**, 187–202 (1980).
39. Margrie, T.W., Brecht, M. & Sakmann, B. In vivo, low-resistance, whole-cell recordings from neurons in the anaesthetized and awake mammalian brain. *Pflügers Arch.* **444**, 491–498 (2002).
40. Klink, R. & Alonso, A. Morphological characteristics of layer II projection neurons in the rat medial entorhinal cortex. *Hippocampus* **7**, 571–583 (1997).
41. Kempter, R., Leibold, C., Buzsáki, G., Diba, K. & Schmidt, R. Quantifying circular-linear associations: hippocampal phase precession. *J. Neurosci. Methods* **207**, 113–124 (2012).
42. Carnevale, N.T. & Hines, M.L. *The NEURON Book* (Cambridge University Press, 2006).
43. Fransén, E., Alonso, A.A., Dickson, C.T., Magistretti, J. & Hasselmo, M.E. Ionic mechanisms in the generation of subthreshold oscillations and action potential clustering in entorhinal layer II stellate neurons. *Hippocampus* **14**, 368–384 (2004).
44. Katz, Y. *et al.* Synapse distribution suggests a two-stage model of dendritic integration in CA1 pyramidal neurons. *Neuron* **63**, 171–177 (2009).